

On the strengthening behavior of ultrafine-grained nickel processed from nanopowders

Q.H. Bui^a, G. Dirras^{a,*}, S. Ramtani^a, J. Gubicza^b

^a LPMTM-CNRS, Université Paris 13, 99 Avenue J.B. Clément, 93430 Villetaneuse, France

^b Department of Materials Physics, Eötvös Loránd University, Budapest, P.O.B. 32, H-1518, Hungary

ARTICLE INFO

Article history:

Received 30 November 2009

Received in revised form 28 January 2010

Accepted 1 February 2010

Keywords:

Nickel

Ultrafine-grains

Spark plasma sintering

Microstructure

Mechanical properties

Hall–Petch relation

ABSTRACT

Bulk ultrafine-grained nickel specimens having grain sizes in the range of 0.25–5 μm were processed by a spark plasma sintering method. The resulting microstructures were characterized by electron backscattering diffraction, transmission electron microscopy and X-ray diffraction analysis. Compression tests were carried out at room temperature and at a strain rate of $1.6 \times 10^{-4} \text{ s}^{-1}$. It was found that the fine-grained microstructure and the presence of NiO phase were the main strengthening factors in the as-processed bulk materials. The contribution of the oxide phase to strengthening was even more pronounced for lower grain sizes. This contribution was calculated as the difference between the measured strength and the value obtained from a Hall–Petch plot of oxide-free samples, and this yielded a flow stress increment of about 635 MPa for the lowest grain size studied here. In addition, a transition from work-hardening to -softening occurred for materials having a mean grain size smaller than about 300 nm and having boundaries that could have been weakened by the presence of a high amount of NiO phase.

© 2010 Elsevier B.V. All rights reserved.

1. Introduction

It is well-known that nanocrystalline (NC) and ultrafine-grained (UFG) materials have superior mechanical strengths compared to their conventional coarse-grained (CG) counterparts [1–4]. There are various processing techniques to fabricate these materials, including electrodeposition (ED) [5,6], severe plastic deformations (SPD) [2,7], powder metallurgy-based methods such as inert gas condensation (IGC) [1,8] and hot isostatic pressing (HIP) [3,4]. Recently, much attention has been paid to the novel spark plasma sintering (SPS) processing technique [9–11]. The most important advantages of the SPS processing route compared to the HIP method are the much shorter duration and the lower temperature of the processing, which limit grain growth during consolidation [12].

UFG nickel (Ni) materials with high strengths and relatively good ductilities may have large-scale industrial applications, particularly in microsystems [13–15] and in nuclear steam generators [16]. Such UFG Ni microstructures have been successfully processed by SPD processing [17,18], ED processing in the form of sheets or thin films [19,20], IGC [21], HIP [22,23] and recently by SPS [9,23] in bulk form. For the specimens processed by SPS, the NiO secondary

phase formed mainly due to powder handling in the consolidation process may have a significant effect on the mechanical properties such as the strength and ductility. Therefore, an in-depth study of the relationship between the microstructure and mechanical properties of SPS-processed samples is necessary, as the disregard of the effect of the oxide phase may lead to the wrong evaluation of the grain size strengthening.

In the present study, the SPS technique is used to process three different Ni microstructures from three types of Ni powders with nominal particle sizes of 50 nm, 100 nm and 5 μm. The microstructure (grain size, grain size distribution, crystallographic texture, defects) of the consolidated materials are characterized and compared using different techniques such as electron backscattering diffraction (EBSD), transmission electron microscopy (TEM) and X-ray diffraction (XRD). The mechanical responses under quasi-static compression tests at room temperature (RT), and the strengthening mechanisms are discussed in accordance with the microstructure characteristics and their evolutions upon straining.

2. Experimental procedures

High purity (~99.99%) Ni nanopowders supplied by the Argonide Corporation (Sanford, Florida) were obtained from the electro-explosion of Ni wires [24,25]. Two nanopowders having spherical particles with nominal sizes of about 50 and 100 nm, as

* Corresponding author. Tel.: +33 1 49 40 34 88; fax: +33 1 49 40 39 38.

E-mail address: dirras@univ-paris13.fr (G. Dirras).

Table 1
Sintering conditions and the density of the as-processed samples.

	Initial powder [nm]	SPS conditions			Density [g/cm ³]	Relative density [%]
		T [°C]	P [MPa]	t [min]		
SPS-A	50	500	150	1	8.40	94.47
SPS-B	100	500	150	1	8.50	95.53
SPS-C	100	500	100	4	8.37	94.00
SPS-D	100	500	100	2	8.61	96.75
SPS-CG	5000	550	150	1.5	8.70	98.00

shown by former TEM investigations [26], were used. In the initial powders, the relative frequency of twin boundaries among the (1 1 1) lattice planes was about 2–3%, as determined from the twin spacings in the TEM images. An energy-filtered TEM investigation showed the presence of an oxygen-containing phase forming a 2 nm thick layer on the particles' surface. This phase was identified by X-ray diffraction as a face-centered cubic (fcc) NiO structure [23].

The powders were consolidated by SPS technique. The SPS procedure was carried out using a Sumitomo S2080 apparatus, which is located at the CNRS platform facility at CIRIMAT (Toulouse, France). SPS was performed in the temperature range of 500–550 °C, with a holding time of 1–4 min. The applied pressure was set between 100 and 150 MPa. Disks of 8 or 50 mm diameter and about 3 mm thick were produced [9]. Table 1 summarizes the optimized processing parameters for the different samples: SPS-A, SPS (-B, -C and -D) and SPS-CG were consolidated from the powders having mean particle sizes of 50 nm, 100 nm and 5 μm, respectively. Samples SPS-B, -C and -D were sintered from the same powder but for different periods of time (see Table 1). The measurement of mass density of the consolidated samples was performed in accordance with Archimedes' principles using distilled water as the immersion medium at room temperature.

The microstructure of the samples before and after deformation was characterized by TEM, SEM and EBSD techniques. A JEOL-2011 electron microscope operating at 200 kV was used for the TEM investigations. Thin foils for TEM were prepared using a Gatan precision ion polishing system (PIPS), with a current of 0.5 mA and a voltage of 5 kV at starting angles of ±7°. Grain boundaries of approximately 400 grains were depicted manually with IMAGE TOOL software using TEM bright field images to determine the grain area (*A*). The grain size was calculated as $d = \sqrt{4A/\pi}$. The relative volume fraction of twinned grains was determined and the twin spacing was also measured by TEM. The EBSD experiments were carried out on a Leo S340 scanning electron microscope. Before EBSD analysis, samples were electropolished using an A2 electropolishing solution from Struers at a voltage of 12 V for 15 s. The EBSD investigations were carried out using a step size of 200 nm.

The grain size and the grain boundary misorientation distributions were determined using an orientation imaging microscopy (OIM) software from TSL.

Prismatic samples with dimensions of 3 mm × 3 mm × 3 mm were cut from the sintered materials for mechanical tests. An Instron universal testing machine (model 1195) was used for the uniaxial compressive tests at room temperature and at a strain rate of $1.6 \times 10^{-4} \text{ s}^{-1}$. In addition, strain rate jump tests were also performed within the strain rate range of 1.6×10^{-4} – $1.6 \times 10^{-2} \text{ s}^{-1}$ to determine the strain rate sensitivity parameter, *m*, and the activation volume, *v*^{*}, of the rate-controlling deformation mechanism. The yield strength at 0.2% offset was computed from the true stress–true plastic strain curve.

3. Results

3.1. Microstructure

The measured and relative mass densities are listed in Table 1. Sample SPS-CG exhibits the highest density among the five samples. The density of sample SPS-A, which was consolidated from the 50 nm powder, is the smallest. This can be attributed to the higher NiO content of this sample, as confirmed by XRD investigations. The X-ray diffractograms for samples SPS-A and SPS-B are shown in Fig. 1. Besides the peak belonging to the Ni phase, additional peaks related to the NiO phase are also present. In order to compare the NiO phase content in the different samples, the intensity ratio of the NiO and Ni peaks at $2\theta = 37.4^\circ$ and 44.6° , respectively, was determined and listed in Table 2. It is noticed that this ratio does not give the NiO phase content in the sample. It is only proportional to the volume fraction of the NiO phase, as previously discussed [23]. The intensity ratios characterizing the oxide content in samples SPS-A, -B, -C and -D were found to be 1.5, 0.9, 0.6 and 0.5%, respectively. No significant amount of NiO phase was identified for sample SPS-CG. At the same time, the intensity ratios characterizing the oxide content in the initial powders having particle sizes of 50 and 100 nm were 1.2 and 0.5%, respectively. The difference between the oxide contents obtained before and after sintering indicates that

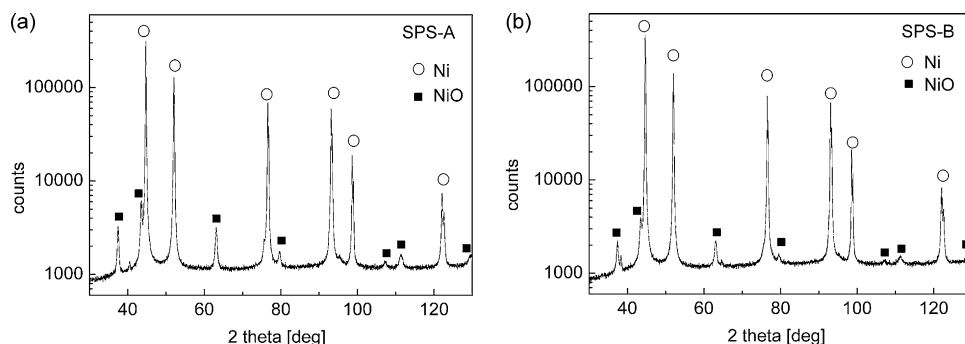


Fig. 1. The X-ray diffractograms of samples (a) SPS-A and (b) SPS-B consolidated from initial powders with the nominal particle sizes of 50 and 100 nm, respectively.

Table 2

Microstructural parameters of the as-processed samples. D_{TEM} , D_{EBSD} and D_{powder} are the grain sizes determined by TEM and EBSD for the sintered samples, and for the initial powders, respectively. f_{twin} is the relative fraction of the twinned grains. $I_{\text{NiO}}/I_{\text{Ni}}$ is the intensity ratio of NiO and Ni peaks at $2\theta = 37.4^\circ$ and 44.6° , respectively, in the X-ray diffractogram.

	D_{TEM} [nm]	D_{EBSD} [nm]	$D_{\text{TEM}}/D_{\text{powder}}$	f_{twin} [%]	Twin spacing [nm]	$I_{\text{NiO}}/I_{\text{Ni}}$ [%]
SPS-A	250	370	5	16.7	35	1.5
SPS-B	294	650	2.94	17.8	30	0.9
SPS-C	306	700	3.06	17.6	39	0.6
SPS-D	318	714	3.18	17.0	38	0.5

additional NiO phase was formed during powder handling before SPS operation or during consolidation. Actually, before SPS operation, the capsule containing the powder was broken in air (SPS-B) or in a controlled Argon atmosphere (SPS-C and SPS-D). This may partially explain the lower oxide contents of samples SPS-C and -D.

In addition, it is noted that the smaller the particle size, the higher the oxide content. This is due to the fact that a smaller particle has a higher specific surface area. Consequently, the lower density of NiO (6.67 g/cm^3) compared to Ni (8.902 g/cm^3) results in a decrease of the relative density of the samples with increasing NiO content.

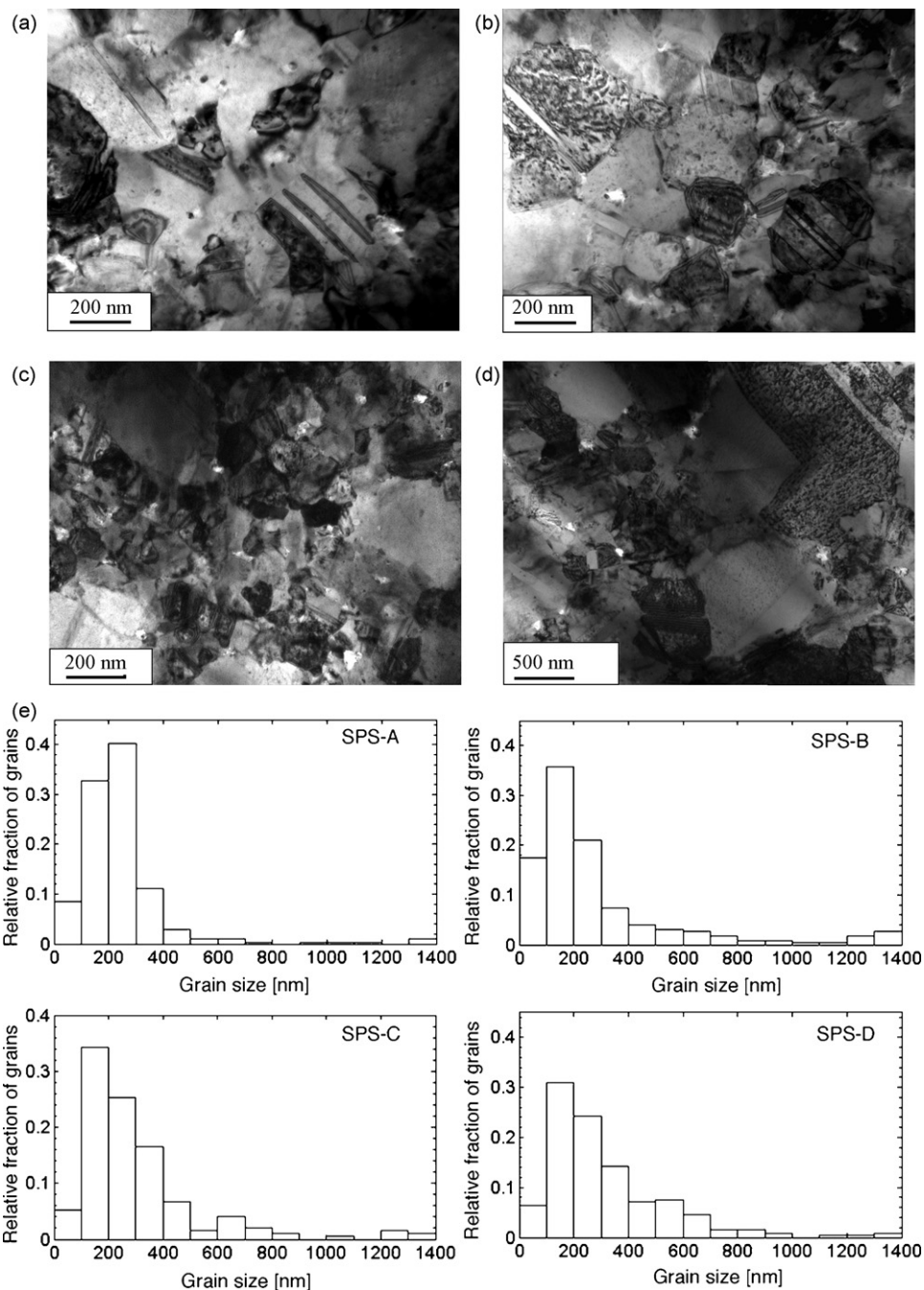


Fig. 2. TEM images (a–d) and grain size distribution (e) of the bulk samples processed by SPS. (a) SPS-A, (b) SPS-B, (c) SPS-C and (d) SPS-D.

However, sample SPS-C possesses a slightly lower relative mass density (94%) compared to sample SPS-B (95.53%), despite its lower oxide content (0.6% for sample SPS-C compared to 0.9% for sample SPS-B). This is probably due to the density heterogeneity through the sample, as the SPS-C disk has a larger diameter (50 mm) compared to SPS-B (8 mm). In addition, a through-thickness density heterogeneity has been reported in a previous work [9].

Fig. 2a–d shows TEM images of samples SPS-A, -B, -C and -D, respectively. The microstructures consist of equiaxed grains and nanotwins. The relative fraction of twinned grains determined by the TEM images is about 17%, and the average twin width is about 40 nm, regardless of the samples (see Table 2). The grain size distributions determined by TEM for the different samples are presented in Fig. 2e. The mean grain sizes for samples SPS-A, -B, -C and -D are 250, 294, 306 and 318 nm, respectively. It is found that the mean grain size values for the consolidated samples are about 3–5 times larger than the mean particle sizes in the initial powders (see Table 2), indicating that the high temperature consolidation resulted in grain coarsening, in agreement with previous reports [10,27]. For samples SPS-B, -C and -D, the differences in the SPS conditions result in detectable changes in the microstructure. For instance, it is observed that samples SPS-C and -D exhibit a higher degree of grain coarsening than sample SPS-B. Quantitative measurements show that the relative fractions of grains with sizes larger than 200 nm are 64 and 46% for samples SPS-D and -B, respectively (see Fig. 2e).

As reported in our previous works [4,22], the microstructure of the as-processed samples is heterogeneous and consists of a matrix of UFG grains and embedded micrometer-sized grains. Some of these coarse grains are subdivided into smaller grain blocks while still keeping more or less their initial spherical shape. Additionally, the microstructure exhibits a random crystallographic texture, and the fraction of high-angle grain boundaries (HAGBs) that have misorientations higher than 15° is high (about 85%) as expected from the applied powder metallurgy processing route. Fig. 3a shows the distributions of misorientation angles across the boundaries for specimens SPS-A and -D. A peak appears at an angle of 60° for both samples, indicating the presence of $\Sigma 3$ boundaries such as coherent twin boundaries [23]. The presence of these twin boundaries is confirmed by the TEM investigations, as shown in Fig. 2, and also by the XRD analysis reported in a recent investigation [9]. By dividing the grain size distribution obtained by OIM into two parts containing the micrometer-sized grains ($d \geq 1 \mu\text{m}$) and the ultrafine-grains ($d < 1 \mu\text{m}$), it is found that the area fraction of the micrometer-sized grains in samples SPS-C and -D is higher (about 50% for both cases) than that in specimen SPS-B (about 40%). The grain size distributions determined by OIM for specimens SPS-A and -D are presented in Fig. 3b. The computed average grain sizes are 370, 650, 700 and 714 nm for samples SPS-A, -B, -C and -D, respectively (see also Table 2). These values are about 1.5–2 times larger than those determined by TEM, as in the EBSD scans the grains that are smaller than the step size (200 nm) have not been counted.

3.2. Mechanical properties

The bulk SPS-processed samples were tested under compression until failure. The true stress–true plastic strain curves are shown in Fig. 4a. Mechanical characteristics such as the yield strength determined at 0.2% offset, the maximum compressive stress, the strain at maximum stress, the plastic strain to failure and the work of fracture are listed in Table 3. It can be observed that:

- (i) Sample SPS-A has the highest yield strength (1022 MPa), probably due to its highest oxide content and smallest grain size. At the same time, its ductility is very low, as this sample already failed at about 4% of plastic strain.

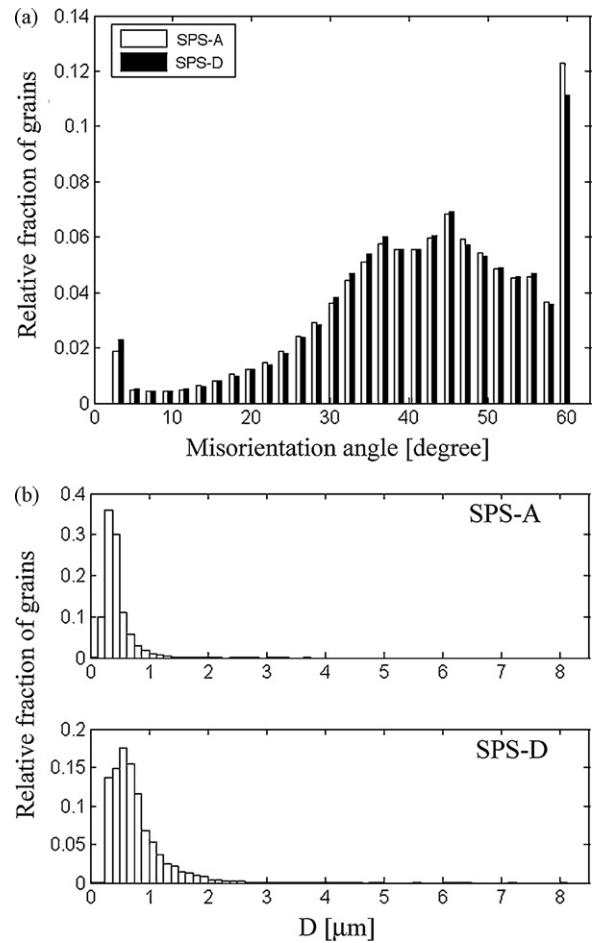


Fig. 3. An illustration of the distribution of the misorientation angles across the boundaries in samples SPS-A and SPS-D (a), the distribution of the grain sizes in samples SPS-A and SPS-D measured by EBSD technique (b). See the text for more details.

- (ii) The yield strength and the ductility of sample SPS-B are about 1.5 times smaller and 5 times higher, respectively, than those of sample SPS-A. This difference can be explained by the higher fraction of large grains (see Fig. 2e) and the lower NiO content in sample SPS-B compared to specimen SPS-A.
- (iii) As expected from their microstructure characteristics, the true stress–plastic strain curves of samples SPS-C and -D are identical. The strain to failure is about 35%, due to the increase of the fraction of micrometer-sized grains compared to samples SPS-A and -B.
- (iv) More generally, the yield strength values of samples SPS-B, -C and -D are about 1.5 times smaller than that of sample SPS-A. At the same time, these strength values are about 7 times larger than that of sample SPS-CG. The lower strength of sample SPS-CG is probably due to the larger grain size and the very small amount of oxide phase within the consolidated sample.

Fig. 4b and c shows the work-hardening rate, Θ , plotted against the applied stress. The work-hardening rate is defined as $\Theta = (\partial\sigma/\partial\varepsilon)_\varepsilon$, and it depends on the dislocation density, the strain rate and temperature of deformation [28]. It can be observed that a transition from work-hardening to work-softening occurs at the maximum stresses of 1178 MPa (at $\varepsilon = 0.01$), 873 MPa (at $\varepsilon = 0.035$), 878 MPa (at $\varepsilon = 0.28$) and 880 MPa (at $\varepsilon = 0.35$) for samples SPS-A, -B, -C and -D, respectively. As indicated in Fig. 4b and c, the values of the linear work-softening rate are about 1500 and 460 MPa for samples

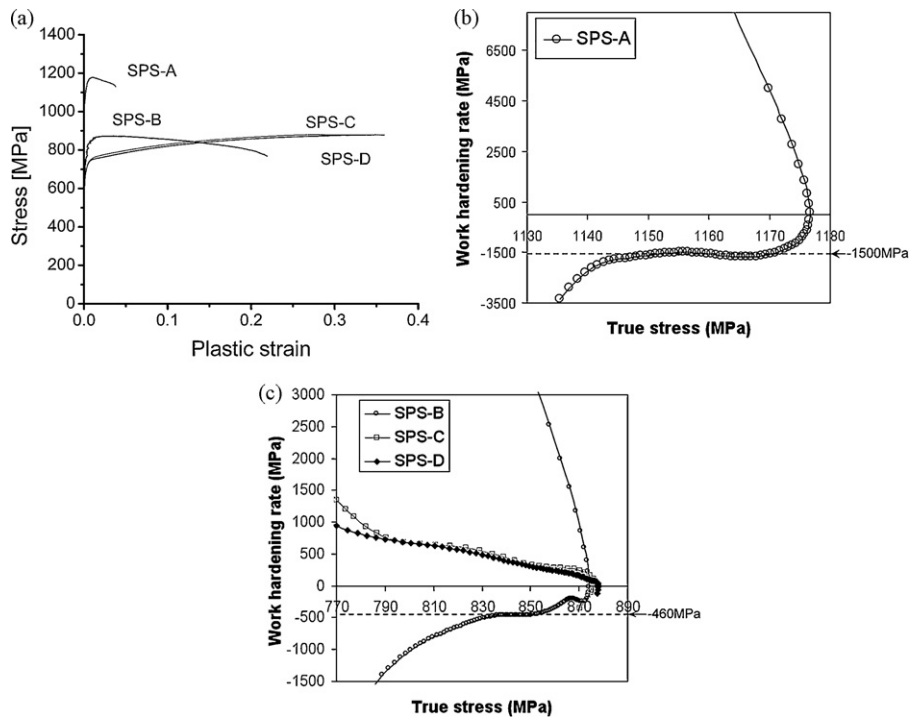


Fig. 4. True stress–true plastic strain curves showing the room temperature compression behavior of the SPS-processed samples at a strain rate of $1.6 \times 10^{-4} \text{ s}^{-1}$ (a); evolution of the hardening rate of samples SPS-A (b) and SPS-B, -C and -D (c).

Table 3
Mechanical characteristics of the HIP-processed [26] and SPS-processed materials.

	HIP-A [26]	HIP-B [26]	HIP-CG [26]	SPS-A	SPS-B	SPS-C	SPS-D	SPS-CG
Yield strength (MPa)	559	530	96	1022	682	660	659	95
Maximum stress (MPa)	784	789	566	1178	873	878	880	566
Strain at maximum stress	0.22	0.34	0.46	0.01	0.035	0.28	0.35	0.46
Failure plastic strain	0.22	0.34	>0.5	0.04	0.21	0.33	0.36	>0.5
WoF (MJ/m ³)	153.76	240.01	225	43.35	183.86	281.66	301.06	211

SPS-A and -B, respectively. The Θ vs. stress curves for samples SPS-C and -D exhibit only negligible softening. For example, in the case of sample SPS-D, the transition from work-hardening to softening is very remote and occurs at the strain of 35%, which is close to the strain at failure (36%) of that sample. Relatively long strain regimes of softening are observed only for samples SPS-A and -B, where the grain size is the smallest and the NiO content is the largest among the five specimens studied here. Moreover, the lower the mean grain size and higher the NiO content, the lower the strain at which the transition from hardening to softening occurs. Therefore, this transition is probably associated with the grain boundary response (e.g. grain boundary decohesion) to the imposed strain during the compression test.

The work of fracture (WoF) of the SPS-processed samples was also determined from the compression tests. This quantity gives the plastic work exerted until fracture, corresponding to the area under the stress–strain curve, and characterizes the toughness of the material [29]. The WoF values for samples SPS-C and -D are much larger than that of samples SPS-A and -B (see Table 3). Indeed, the WoF values for samples SPS-C and -D are close to each other, and they are about 7 and 1.6 times higher than the values for samples SPS-A and -B, respectively. This can mainly be attributed to the larger compressive ductility (defined here as the strain at failure during the compression test) of samples SPS-C and -D. The results clearly reveal the enhanced damage tolerant capability of samples SPS-C and -D.

3.2.1. The strain rate sensitivity of the flow stress and the activation volume

The strain rate sensitivity $m = \partial \ln \sigma / \partial \ln \dot{\epsilon}$ and the apparent activation volume $v^* = k_B T (\partial \ln \dot{\epsilon} / \partial \ln \sigma)_T$ were determined by strain rate jump tests in the strain rate regime from 1.6×10^{-4} to $1.6 \times 10^{-2} \text{ s}^{-1}$ at RT. The measured values of m and v^* for the different samples are shown in Table 4. The results show that m increases and v^* decreases with decreasing grain size, in agreement with previous reports (e.g. [30]). The value of m varies from 0.0086 (in the case of sample SPS-A) to 0.005 (for specimen SPS-CG), and the corresponding activation volumes are 61 and 213 b³, respectively.

Fig. 5 shows a comparison between the values of the strain rate sensitivity parameter measured here and those reported in previous works [30–34]. The strain rate sensitivity for UFG fcc materials has been found to be significantly higher than that of CG materi-

Table 4

The values of the strain rate sensitivity of the flow stress m and activation volume v^* (b³) measured at RT for the samples having different grain sizes.

	SPS-A	SPS-B	SPS-D	SPS-CG
Grain size	250 nm	294 nm	318 nm	50 μm
m	0.0086 ^a	0.0077 ^{a,b}	0.0069 ^b	0.005 ^b
v^* (b ³)	61.35	61.83	78.49	212.86

^a Measured in compression testing at two different constant strain rates.

^b Measured in strain rate jump tests.

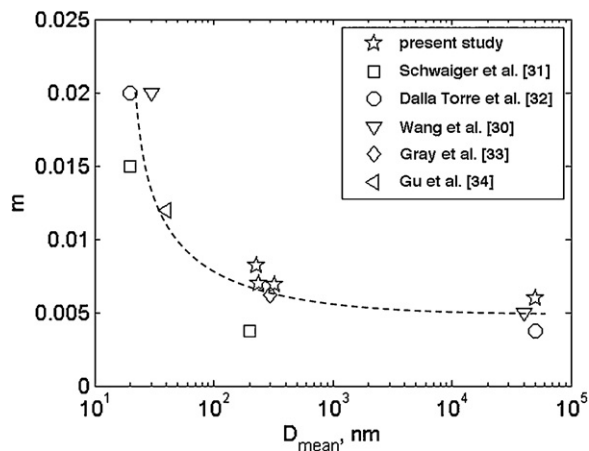


Fig. 5. Comparison of the grain size dependence of the strain rate sensitivity for the SPS-processed samples studied here and for the data taken from the literature (Schwaiger et al. [31], Dalla Torre et al. [32], Wang and Ma [30], Gray et al. [33], Gu et al. [34]).

als, and it has been between the values typical for grain boundary sliding and mutual dislocation trapping. Actually, a relatively high value of strain rate sensitivity ($m=0.02$) has been obtained for NC Ni [32], and the operation of both grain boundary dislocation activity and grain boundary sliding has been suggested. In the present study, the measured activation volumes appear too high for reflecting a deformation mechanism involving grain boundary sliding. Indeed, the measured activation volume for the material having the smallest grain size (SPS-A) is $61 b^3$, which is higher than that of NC Ni ($50 b^3$) [28]. Therefore, in the case of UFG Ni studied here, the deformation mechanisms are related rather to the activity of lattice dislocations and their interactions with grain boundaries and

other obstacles. The higher concentration of glide obstacles (such as forest dislocations, oxide particles and grain boundaries) with decreasing grain size may reduce the activation area for dislocations motion, which is the area swept by a dislocation overcoming obstacles in its course. As in the case of dislocations, the activation volume is the product of the activation area and the Burgers vector; therefore, the smaller the activation area, the smaller the activation volume.

3.3. Deformed microstructure

The microstructures of the different materials after compression tests at RT were characterized by combining SEM and EBSD investigations. The results are presented in the following.

3.3.1. Surface of the deformed samples studied by SEM

Fig. 6a and b shows SEM images of the surface of sample SPS-B deformed up to the strain values of 7 and 10%, respectively. The black arrows (in Fig. 6a) indicate the loading axis. In Fig. 6a, a shear band (indicated by two black lines) is observed that formed along the maximum shear stress planes and is inclined at an angle of approximately $\sim 50^\circ$ to the compression axis. It can also be seen that the deformed microstructure of the UFG Ni is heterogeneous and that the number of shear bands increases with the increase of plastic strain, as shown in Fig. 6b. The operation of shear bands is clearly evidenced by the displacement of scratches formed during the polishing of the sample, the concentration of which increases with increasing strain (Fig. 6b). In addition, it was observed in a previous work [23] that upon straining, cracks occurred mainly at the boundaries of large grains located within the shear bands. The concentration and length of these cracks increased with increasing strain. This may very well explain the softening of sample SPS-B during the quasi-static compression tests at RT.

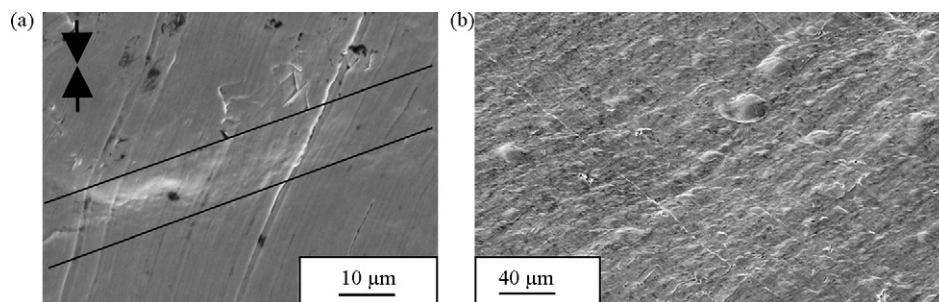


Fig. 6. SEM micrographs showing the surface of sample SPS-B deformed by compression at RT and at strains of about 7% (a) and 10% (b). A macroscopic shear band delineated by black lines is indicated in (a), and numerous slip bands are observed in (b). The arrows in (a) indicate the compression direction.

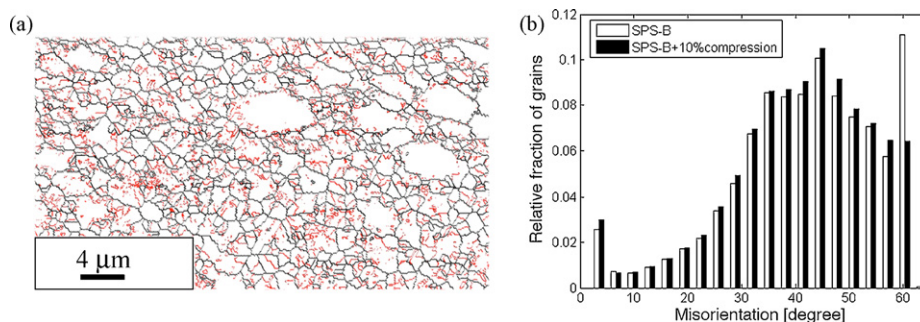


Fig. 7. EBSD boundary map for sample SPS-B after plastic deformation at a strain of 10%. The red and black lines represent the low-angle grain boundaries with misorientations between 2° and 15° and the high-angle grain boundaries with larger misorientations, respectively (a); the distribution of the misorientation angles across the boundaries in sample SPS-B in the initial state and after deformation (b). (For interpretation of the references to color in the citation of this figure, the reader is referred to the web version of the article.)

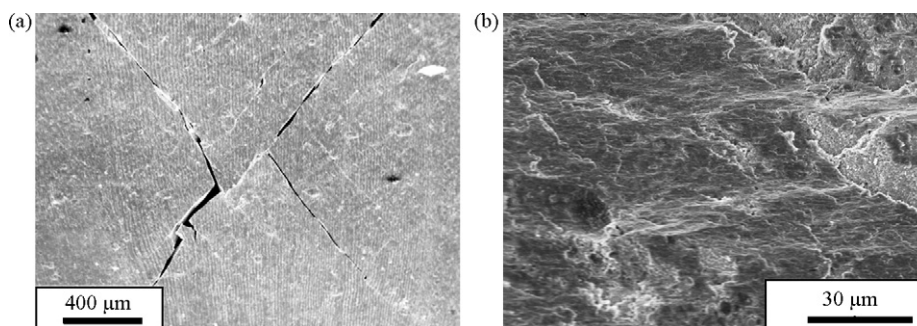


Fig. 8. SEM micrographs showing macroscopic cracks on the lateral surface (a), and the structure of the fractured surface for sample SPS-B (b).

3.3.2. Surface of the deformed samples analyzed by EBSD

Fig. 7a illustrates the microstructure of sample SPS-B at a compressive strain of about 10%. It is noted that the change of the shape of CG grains is more significant than that of UFG grains. This can be explained by a localized deformation occurring in the vicinity of the softer CG regions. In Fig. 7a, the red and black lines represent the LAGBs (low-angle grain boundaries) and HAGBs, respectively. The distributions of the misorientation angles for sample SPS-B before and after compression are compared in Fig. 7b. For the as-processed sample, there is a peak at approximately 60° , which is attributed to $\Sigma 3$ coincident-site lattice twin boundaries. After 10% plastic strain, the $\Sigma 3$ peak disappears, indicating the reduction of the relative frequency of twin boundaries. At the same time, an increase of the fraction of LAGBs is observed. The untwinning and the increase of the fraction of LAGBs can be explained by the activity of dislocations.

3.3.3. Fracture behavior

After the compression test, it is observed that the majority of SPS-processed samples splits into two parts. The fractured surfaces were inclined at an angle of about $45\text{--}60^\circ$ to the compression axis, as shown in Fig. 8a taken on sample SPS-B. This angle corresponds to the inclination angle of shear bands to the compression axis as described above. In addition, Fig. 8b shows that while microvoids can be observed in some areas, a large fraction of the surface appears to be smooth without microvoids or cavities, which are characteristics of a ductile fracture. Therefore, the failure of the samples studied here occurred mainly by a brittle-like fracture, most probably along grain boundaries (GBs; intergranular fracture), in agreement with the report of Cao et al. [4].

4. Discussion

4.1. UFG Ni consolidated by two different powder metallurgy routes

In order to evaluate the influence of processing route on the mechanical properties of UFG Ni samples, the true stress–plastic strain curves of the SPS-processed samples were compared with those of HIP-processed samples. These HIP-processed samples were consolidated from the same powders as those used for the SPS samples. The HIP-processed samples consolidated from the 50 and 100 nm Ni powders yielded average grain sizes of about 333 and 403 nm (measured by TEM), respectively. These samples were designated as HIP-A and HIP-B, respectively. The samples consolidated by HIP had lower oxide contents compared to the SPS-processed samples studied here [23]. It was revealed [23] that the oxide contents of the HIP-processed samples were the same as those of the initial powders (1.2 and 0.5% for the powders having particle sizes of 50 and 100 nm, respectively), indicating that additional NiO was not formed during the HIP procedure. A more detailed description of

the microstructure of the HIP-processed samples can also be found in a recent work [26].

Fig. 9 shows the true stress vs. plastic strain curves obtained by compression at a strain rate of $1.6 \times 10^{-4} \text{ s}^{-1}$ and at RT for three specimens processed by HIP and having different grain sizes [26]. All of the HIP-processed samples exhibited work-hardening up to a large plastic strain value, in contrast to the SPS-processed samples, thus showing that different degrees of work-softening depend on the grain size (therefore on the mean particle size in the initial powder). The smaller the particle size in the initial powder, the higher the amount of NiO phase in the SPS-processed samples. Most probably, the oxide phase localized within GBs and triple junctions during sintering [23]. EBSD investigations showed that GBs are intensely involved in plastic deformation. Therefore, the deposition of oxide dispersions within the boundaries or triple junctions might weaken these boundaries and result in softening due to intergranular failure. At the same time, the HIP-processing was carried out under a controlled Ar atmosphere, thereby reducing the oxide content of the samples consolidated by this procedure.

To further study the effect of both grain size and oxide content on the strengthening, the mechanical characteristics of the HIP-processed samples were also investigated, as listed in Table 3. The plastic strain at failure for sample HIP-B was close to the values obtained for samples SPS-C and D processed from the same powder.

4.2. Effect of the oxide content on the strength of UFG nickel

The contribution of grain refinement to the strength of materials can be expressed by the empirical Hall–Petch relationship [35,36]. It is generally accepted that for conventional polycrystals with micrometer-sized grains, the yield strength of polycrystalline materials is proportional to the inverse square root of the mean

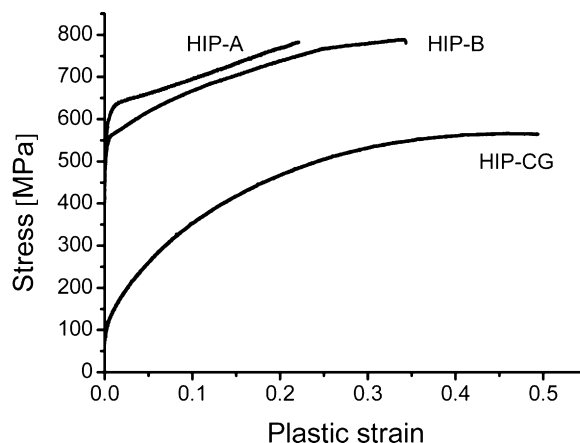


Fig. 9. Room temperature compression behavior of HIP-processed Ni samples taken from Ref. [26] (HIP-A: 333 nm; HIP-B: 403 nm; HIP-CG: 5 μm).

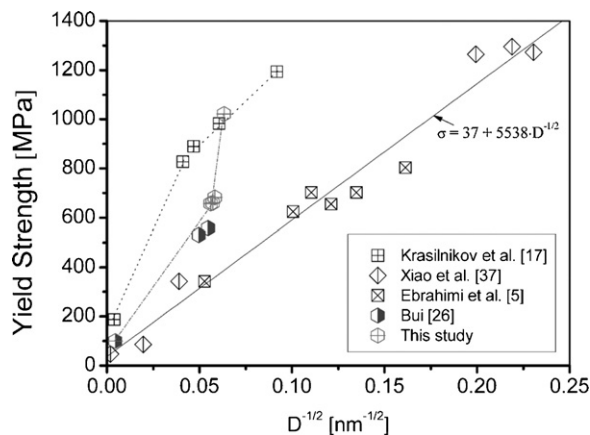


Fig. 10. Hall–Petch relation for nickel fabricated by different processing routes. The solid line represents a linear fit on data taken from Refs. [37] and [5].

grain size, i.e., $\sigma = \sigma_0 + kD^{-1/2}$, where σ is the yield strength, σ_0 is the friction stress, k is a constant referred to as Hall–Petch slope and D is the mean grain size. Fig. 10 shows the Hall–Petch plot of the data published in the literature [5,17,26,37] and obtained in the present study. The data taken from Refs. [5] and [37], where the samples were processed by ED, can be fitted well by a Hall–Petch relationship with $\sigma_0 = 37$ MPa and $k = 5538$ nm^{1/2}. At the same time, Fig. 10 shows that the data taken from Ref. [17] strongly deviate from the Hall–Petch behavior. Based on a previous analysis by Hughes and Hansen [38], the authors Krasilnikov et al. [17] attributed the observed behavior to an additional strengthening effect introduced by the presence of substructures, such as geometrically necessary boundaries and trapped lattice dislocations, in the vicinity of grain boundaries. These substructures were formed due to the SPD processing routes, which is not the case for ED, HIP and SPS processing methods. Nevertheless, for the samples processed by HIP [26] and SPS (red symbols in Fig. 10), a deviation from the Hall–Petch behavior was also observed. This deviation was even more pronounced for the SPS-processed samples and particularly for the sample processed from the powder having the smallest particle size (SPS-A). This effect is most probably due to the higher oxide content at lower grain sizes, whose origin was discussed above. Assuming a simple linear addition of the strength contributions from the grain size and the oxide particles, the oxide strengthening can be estimated by subtracting the strength contribution of the grain size from the experimental yield strength. The strength caused by the grain size can be approximated from the Hall–Petch relationship obtained for the oxide-free samples processed by ED (see Fig. 10). This calculation gives the contribution of the oxide phase to strength as: $\Delta\sigma_{\text{SPS-A}} = 635$ MPa, $\Delta\sigma_{\text{SPS-B}} = 322$ MPa, $\Delta\sigma_{\text{SPS-C}} = 306$ MPa and $\Delta\sigma_{\text{SPS-D}} = 311$ MPa for samples SPS-A, -B, -C and -D, respectively.

Assuming that the contribution of oxide dispersoids to the strength is proportional to the oxide content determined by XRD, the data obtained for sample SPS-A suggested that an oxide content of 1% would induce an increase in the strength of about 423 MPa. Using the values of oxide content listed in Table 2, one would expect about $\Delta\sigma_{\text{SPS-B}} = 381$ MPa, $\Delta\sigma_{\text{SPS-C}} = 254$ MPa and $\Delta\sigma_{\text{SPS-D}} = 211$ MPa for samples SPS-B, -C and -D, respectively. The deviation of these values from the experimentally determined strength contributions of the oxide phase can be attributed to the fact that the strengthening effect of oxide particles depends not only on their volume fraction but also on their size, which may be different for the various SPS-processed samples. It can be concluded that the strength contribution of the oxide content may lead to a deviation from the Hall–Petch relationship, which will no longer solely reflect the grain size effect. In accordance with pre-

vious observations [17], the present results also suggest that the deviations observed in the Hall–Petch plots proposed in the literature are mainly due to the differences in the processing routes, which may induce differences in the microstructure. The influence of oxide content on the yield strength of metallic materials has been also emphasized in previous works [10,39].

5. Conclusions

Near fully dense, ultrafine-grained Ni samples with different average grain sizes were successfully consolidated using spark plasma sintering and were mechanically tested in quasi-static compressive test conditions at RT. It was observed that:

- (i) A transition in the strain hardening behavior, from work-hardening to work-softening occurs, for the SPS-processed materials having a mean grain size smaller than about 300 nm. This transition corresponds to a change in the deformation mode from homogeneous deformation to strain localization in shear bands. The softening is attributed to crack formation inside the shear bands, most probably as a consequence of the high-flow stress level and the weak boundary strength due to the presence of an oxide phase.
- (ii) The yield strength measured at RT does not follow the Hall–Petch law, as a consequence of the presence of the oxide phase, whose strengthening effect superimposes to the contribution of the grain size.
- (iii) The measured strain rate sensitivity parameter and the corresponding activation volume of the UFG Ni samples suggest that lattice dislocations and their interactions with grain boundaries and other obstacles, such as oxide dispersoids, mainly control the deformation.

Acknowledgements

Q.H. Bui is very grateful to Q.B. Nguyen, Department of Mechanical Engineering, National University of Singapore, for fruitful discussions. This work was supported in part by the French National Research Agency, ANR (ANR 09-BLAN-0010-01), as well as the Hungarian Scientific Research Fund, OTKA, Grant No. K 81360.

References

- [1] H. Gleiter, *Prog. Mater. Sci.* 33 (1989) 223–315.
- [2] R.Z. Valiev, R.K. Islamgaliev, I.V. Alexandrov, *Prog. Mater. Sci.* 45 (2000) 103–189.
- [3] S. Billard, J. Fondere, B. Bacroix, G. Dirras, *Acta Mater.* 54 (2006) 411–421.
- [4] W. Cao, G. Dirras, M. Benyoucef, B. Bacroix, *Mater. Sci. Eng. A* 462 (2007) 100–105.
- [5] F. Ebrahimi, G.R. Bourne, M.S. Kelly, T.E. Matthews, *Nanostruct. Mater.* 11 (1999) 343–350.
- [6] C. Cheung, F. Djuanda, U. Erb, G. Palumbo, *Nanostruct. Mater.* 5 (1995) 513–523.
- [7] V.M. Segal, *Mater. Sci. Eng. A* 271 (1999) 322–333.
- [8] V. Haas, H. Gleiter, *Scripta Metall. Mater.* 28 (1993) 721–724.
- [9] G. Dirras, S. Bouvier, J. Gubicza, B. Hasni, T. Szilagyí, *Mater. Sci. Eng. A* 526 (2009) 201–210.
- [10] B. Srinivasarao, K. Oh-ishi, T. Ohkubo, K. Hono, *Acta Mater.* 57 (2009) 3277–3286.
- [11] M. Kubota, *J. Alloys Compd.* 434–435 (2007) 294–297.
- [12] S. Paris, E. Gaffet, F. Bernard, Z.A. Munir, *Scripta Mater.* 50 (2004) 691.
- [13] K.J. Hemker, H. Last, *Mater. Sci. Eng. A* 319–321 (2001) 882–886.
- [14] R.Z. Valiev, R.S. Mishral, J. Grozal, A.K. Mukherjee, *Scripta Mater.* 34 (1996) 1443–1448.
- [15] T.E. Buchhein, D.A. Lavan, J.R. Michael, T.R. Christenson, S.D. Leith, *Metall. Mater. Trans. A* 32A (2002) 539.
- [16] G. Palumbo, F. Gonzalez, A.M. Brennenstuhl, U. Erb, W. Shmayda, P.C. Lichtenberger, *Nanostruct. Mater.* 9 (1997) 737–746.
- [17] N. Krasilnikov, W. Lojkowski, Z. Pakiel, R. Valiev, *Mater. Sci. Eng. A* 397 (2005) 330–337.
- [18] A. Zhilyaev, A. Gimazov, E. Soshnikova, Á. Révész, T. Langdon, *Mater. Sci. Eng. A* 489 (2008) 207–212.
- [19] S.X. McFadden, R.S. Mishra, R.Z. Valiev, A.P. Zhilyaev, A.K. Mukherjee, *Nature* 398 (1999) 684–686.

- [20] A. El-Sherik, J. Shirokoff, U. Erb, J. Alloys Compd. 389 (2005) 140–143.
- [21] H. Kisker, T. Gessmann, R. Wurschum, H. Kronmuller, H. Schaefer, Nanostruct. Mater. 6 (1995) 925–928.
- [22] G. Dirras, J. Gubicza, S. Ramtani, Q.H. Bui, T. Szilágyi, Mater. Sci. Eng. A 527 (2010) 1206–1214.
- [23] J. Gubicza, Q.H. Bui, F. Fellah, G. Dirras, J. Mater. Res. 24 (2009) 217–226.
- [24] F. Tepper, Met. Powder Rep. 53 (1998) 31.
- [25] Y. Kwon, Y. Jung, N.A. Yavorovsky, A.P. Illyin, J. Kim, Scripta Mater. 44 (2001) 2247–2251.
- [26] Q.H. Bui, PhD Thesis, University of Paris 13, Villetaneuse (2008).
- [27] Z. Zhang, F. Wang, L. Wang, S. Li, Mater. Sci. Eng. A 476 (2008) 201–205.
- [28] F. Dalla Torre, P. Spatig, R. Schaublin, M. Victoria, Acta Mater. 53 (2005) 2337–2349.
- [29] Q.B. Nguyen, M. Gupta, Compos. Sci. Technol. 68 (2008) 2185–2192.
- [30] Y.M. Wang, E. Ma, Mater. Sci. Eng. A 375–377 (2004) 46–52.
- [31] R. Schwaiger, B. Moser, M. Dao, N. Chollacoop, S. Suresh, Acta Mater. 51 (2003) 5159–5172.
- [32] F. Dalla Torre, H. Van Swygenhoven, M. Victoria, Acta Mater. 50 (2002) 3957–3970.
- [33] G.T. Gray, T.C. Lowe, C.M. Cady, R.Z. Valiev, I.V. Aleksandrov, Nanostruct. Mater. 9 (1997) 477–480.
- [34] C. Gu, J. Lian, Z. Jiang, Q. Jiang, Scripta Mater. 54 (2006) 579–584.
- [35] E.O. Hall, Proc. Phys. Soc. London B64 (1951) 747–753.
- [36] N.J. Petch, J. Iron Steel Inst. 174 (1953) 25–28.
- [37] C. Xiao, R.A. Mirshams, S.H. Whang, W.M. Yin, Mater. Sci. Eng. A 301 (2001) 35–43.
- [38] D.A. Hughes, N. Hansen, Acta Mater. 48 (2000) 2985–3004.
- [39] J. Gubicza, G. Dirras, P. Szommer, B. Bacroix, Mater. Sci. Eng. A 458 (2007) 385–390.